Bacterial scattering in microfluidic crystal flows reveals giant active Taylor–Aris dispersion

Amin Dehkharghani[a], Nicolas Waisbord[a], Jörn Dunkel[b], and Jeffrey S. Guasto[a,1]

[a]Department of Mechanical Engineering, Tufts University, Medford, MA 02155; and [b]Department of Mathematics, Massachusetts Institute of Technology, Cambridge, MA 02139-4307

The natural habitats of planktonic and swimming microorganisms, from algae in the oceans to bacteria living in soil or intestines, are characterized by highly heterogeneous fluid flows. The complex interplay of flow-field topology, self-propulsion, and porous microstructure is essential to a wide range of biophysical and ecological processes, including marine oxygen production, remineralization of organic matter, and biofilm formation. Although much progress has been made in the understanding of microbial hydrodynamics and surface interactions over the last decade, the dispersion of active suspensions in complex flow environments still poses unsolved fundamental questions that preclude predictive models for microbial transport and spreading under realistic conditions. Here, we combine experiments and simulations to identify the key physical mechanisms and scaling laws governing the dispersal of swimming bacteria in idealized porous media flows. By tracing the scattering dynamics of swimming bacteria in microfluidic crystal lattices, we show that hydrodynamic gradients hinder transverse bacterial dispersion, thereby enhancing stream-wise dispersion ∼100-fold beyond canonical Taylor–Aris dispersion of passive Brownian particles. Our analysis further reveals that hydrodynamic cell reorientation and Lagrangian flow structure induce filamentous density patterns that depend upon the incident angle of the flow and disorder of the medium, in striking analogy to classical light-scattering experiments.

swimming cells | active matter | transport | dispersion | porous media

Scattering experiments have long been used to successfully probe the structure and dynamics of photons, electrons, and other forms of passive matter (1). A recent extension of traditional particle-scattering concepts to living matter has provided important insights into the cell–cell (2, 3) and cell-surface interactions (4–7) of swimming microorganisms in simple scattering geometries and under idealized quiescent fluid conditions. By contrast, very little is known about the individual and collective behaviors of bacteria and other microbes in their natural, highly dynamic, and geometrically complex fluid habitats (8, 9). The biological and ecological importance of cell-flow and cell-surface interactions in porous media and turbulent environments is now widely recognized in the regulation of cell dispersal (10, 11), chemotaxis (11, 12), fertilization (13), biofilm formation (14), and disease transmission (15). However, due to a lack of quantitative data, no validated predictive models exist to describe such processes (16). Here, we combine experiments and simulations to determine the effects of the carrier fluid flow on the transport of swimming bacteria through a periodic microfluidic lattice, drawing inspiration from classical X-ray scattering experiments by Bragg and Laue (1).

The random walks of self-propelled cells and particles in uniformly moving fluids are often described as diffusion (17–19), which enabled early theoretical progress on active transport in flow (20, 21). However, recent experiments (10, 11) showed that even simplistic, 1D flow gradients can cause local cell accumulations (22), with profound implications for microswimmer transport (23–25). Notwithstanding such progress, the mech-

anisms by which generalized fluid flows and self-propulsion can enhance or hinder the densification and dispersion of swimming cells (11) in geometrically complex environments are not yet known (26). Identifying the underlying biophysical and hydrodynamic effects is essential for understanding the dynamics of active suspensions in porous media and turbulent flows, which are often characterized by strong kinematic mixing (27) due to heterogeneous 2D and 3D velocity gradients.

To investigate and quantify how flow gradients and self-propulsion determine the transport properties of active suspensions relative to passive Brownian solutes, we studied the scattering dynamics of swimming bacteria at single-cell resolution in a periodic microfluidic lattice (Fig. 1A). Similar to classical light scattering, our experimental setup allowed us to precisely control the incidence angles of the carrier flows relative to the microfluidic crystal lattice and thus disentangle the effects of hydrodynamic mixing and dispersion often found in disordered systems. In agreement with predictions from a Langevin model, our data reveal a strong dependence of the cell densification patterns and dispersion coefficients on the incident flow angles, which are two key features that we show to persist in biologically relevant random media (*SI Appendix*). While local fluid shear can describe bacterial accumulation in simple, 1D flows (11), our results below illustrate that in generalized, Lagrangian-unsteady flows, advection and the velocity gradient history of the flow regulate the topology of cell distributions. We

---

Significance

The fluid habitats of swimming microbes are characterized by heterogeneous flow, typical of groundwater and marine turbulence, which can augment cell transport in unexpected ways and affect important processes ranging from biogeochemical cycling to disease transmission. Following in the footsteps of century-old light diffraction techniques, the scattering of bacteria in microfluidic crystal flows reveals how cell shape and motility couple to hydrodynamic gradients, giving rise to observed filamentous cell density patterns. Consequently, hindered bacterial mobility transverse to the flow greatly enhances downstream dispersion. These results illustrate the stark contrast of active matter transport with passive Brownian particles and may provide insights into microbial ecosystems, biomedical device design, and the guidance of swimming microrobots.
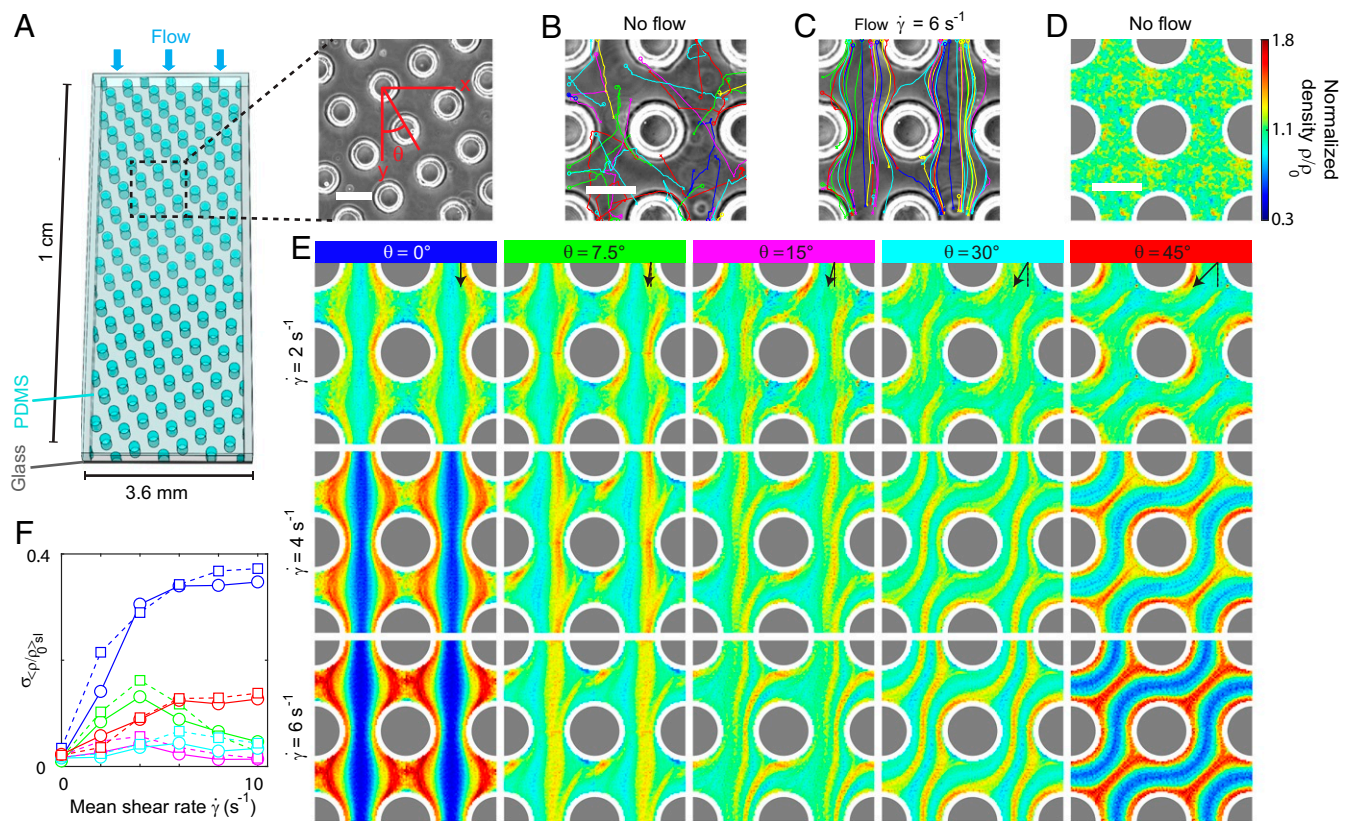
Fig. 1. Swimming bacteria scatter in microfluidic lattice flows forming filamentous density patterns. (*A*) Schematic of the microfluidic device (depth, 100 μm) composed of a square, periodic lattice of circular pillars, oriented at various angles relative to the flow. *Inset* shows annotated channel image ($\theta = 30°$). Pillar diameter (65 μm) and lattice constant (120 μm) are constant for all experiments. (Scale bar, 100 μm.) (*B* and *C*) Sample trajectories of swimming bacteria (*B. subtilis*; $\theta = 0°$) at mean shear rates (*B*) $\dot{\gamma} = 0$ s^{-1} and (*C*) $\dot{\gamma} = 6$ s^{-1}. (Scale bar, 65 μm.) (*D*) Normalized cell density without flow ($\dot{\gamma} = 0$ s^{-1}) showing no large-scale density pattern. Density, ρ, is measured from experiments by binning cell counts (2-μm × 2-μm resolution) and normalized by the mean density, ρ_0 (*Materials and Methods*). White zones around pillars are excluded from analysis due to inconsistent cell detection caused by light scattering. (Scale bar, 65 μm.) (*E*) Experimentally measured cell densities change qualitatively with the incident flow angle, θ, exhibiting filamentous density patterns, whose topology is conserved across mean shear rates, $\dot{\gamma}$. Black arrows indicate mean flow directions (*Top* row), and scale bar and color bar from *D* apply. (*F*) Density contrast (SD of streamline-averaged, normalized cell density) characterizes changes in cell density as a function of shear rate for various lattice angles in experiments (solid lines) and simulations (dashed lines) (*SI Appendix*, Fig. S4).

identify cell alignment to Lagrangian fluid stretching as the primary mechanism for the observed densification. Strikingly, our data further show that cell reorientation, determined by vorticity history, hinders lateral transport and amplifies stream-wise dispersion ~100-fold beyond Taylor–Aris dispersion (28, 29) for passive particles.

Results and Discussion

Bacterial Suspension Flow in a Microfluidic Crystal Lattice. The microfluidic lattices (Fig. 1*A* and *Materials* and *Methods*) comprise a square, periodic array of circular pillars in an otherwise rectangular cross-section microchannel. The pillar diameter (65 μm) and lattice spacing (120 μm) are held constant, and the flow topology is modified by rotating the lattice orientation relative to the mean flow direction (Fig. 1*A*, *Inset*) in a series of five individual channels ($\theta = 0°, 7.5°, 15°, 30°, 45°$; *SI Appendix*, Figs. S1 and S2). A dilute suspension of wild-type *Bacillus subtilis* bacteria (mean swimming speed $V_s = 31.2$ μm/s; *Materials and Methods*) was flowed through the device using a syringe pump in a mean flow speed range of $\bar{U}_f = 0-400$ μm/s, corresponding to a mean shear rate of $\dot{\gamma} = 0-10$ s^{-1}, defined here as the spatial average of the positive eigenvalue of the strain rate tensor (*SI Appendix*, Fig. S1). Results are presented in terms of the mean shear rate, which was shown to be a key parameter in microbial transport (11, 22). Video microscopy captures the

cell motion (Fig. 1 *B* and *C*) and spatial distribution (Fig. 1 *D* and *E*) in the middepth of the microchannel, which was designed with a large channel height to pillar spacing ratio (≈2) to ensure fluid velocity gradients are dominant in the image plane. Measured data are periodically averaged in space and presented as a 2 × 2 tiling of the unit cell (Fig. 1 *D* and *E* and *Materials* and *Methods*).

Bacterial Scattering Yields Angle-Dependent Filamentous Density Patterns. Steady flow through the microfluidic lattice results in striking, filamentous cell density patterns, which meander around pillars (Fig. 1*E*) and along streamlines (Fig. 2*A*). In contrast, nonmotile cells and particles do not exhibit such densification (*SI Appendix*, Fig. S3), and without flow, the random walks of motile bacteria (Fig. 1*B*) generate a homogeneous cell density, ρ, normalized by the mean density, ρ_0 (Fig. 1*D*). Changes in the flow topology (*SI Appendix*, Fig. S1), generated by varying the incident mean flow angle, θ, with respect to the lattice, cause drastic changes in the filament topologies, which track the fluid streamlines (Fig. 2*A*). Filamentous bacterial density patterns are also prominent in biologically relevant random media (*SI Appendix*, Fig. S9). Topological changes in the filament structure with flow angle are accompanied by changes in the density contrast (Fig. 1*F*), which is defined as the SD of the streamline-averaged, normalized
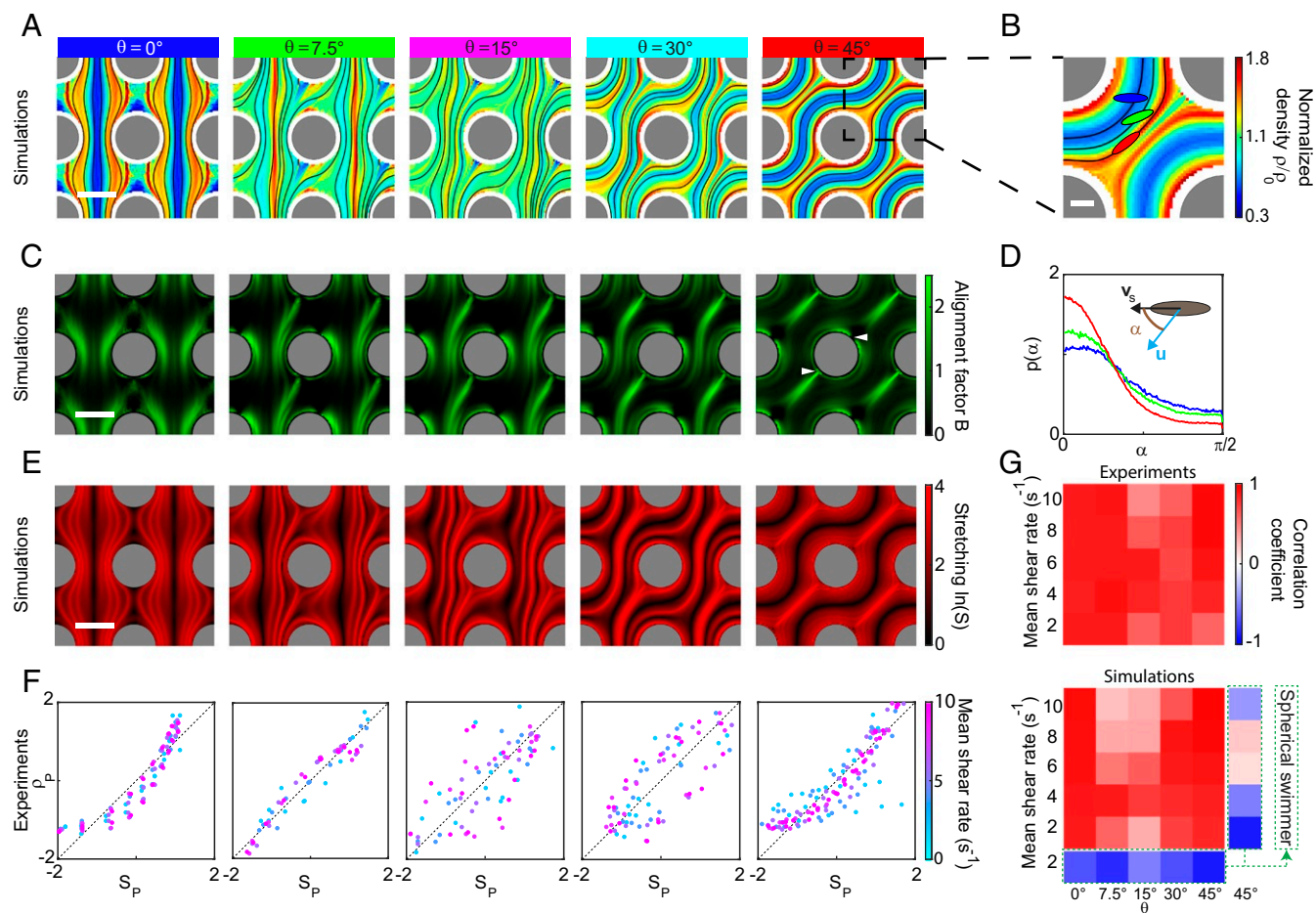
Fig. 2. Hydrodynamic alignment of bacteria drives filamentous density patterns. (*A*) Normalized cell densities from Langevin simulations ($\dot{\gamma} = 6\,\text{s}^{-1}$) capture experimentally observed densification patterns (cf. Fig. 1*E*, *Bottom* row). Black lines are streamlines (constant for all mean shear rates). (Scale bar, 60 μm.) (*B*) Streamlines coincide with bacterial density striations ($\theta = 45°$, $\dot{\gamma} = 6\,\text{s}^{-1}$), where the schematic of elongated cell alignment represents the hypothesized mechanism of densification. (Scale bar, 20 μm.) (*C*) Investigation of cell orientation from simulations (*A*) shows local alignment to extensional zones, but not to the full structure of bacterial filaments. Cell alignment is defined as $B = \sqrt{\langle \alpha_0^2 \rangle / \langle \alpha^2 \rangle} - 1$, where α is the acute angle between cell body and streamline, $\langle \alpha_0^2 \rangle$ is the mean-square angle for a uniform cell orientation distribution, and $\langle \cdot \rangle$ indicates ensemble averaging. White arrowheads highlight hyperbolic flow regions for $\theta = 45°$. (Scale bar, 60 μm.) (*D*) Sample distributions of cell-streamline angle, α, corresponding to streamlines with colored ellipsoids in *B*, illustrate prominent cell alignment on high-density filaments. *Inset* shows schematic of bacterial swimming velocity, $\mathbf{v}_s$, in a flow with fluid velocity $\mathbf{u}$. (*E*) Lagrangian fluid stretching measured from flow fields (*SI Appendix*, Figs. S1 and S2) for lattice angles in *A* with $\dot{\gamma} = 6\,\text{s}^{-1}$. (Scale bar, 60 μm.) (*F*) Scatter plot of Pearson-normalized variables exemplifies the correlation between bacterial density, ρ_P, and stretching, S_P (black dashed line is slope 1). Pearson variables are defined as $X_P = (X - \langle X \rangle)/\sigma(X)$, where X is streamline-averaged logarithm of normalized cell density, $\langle \ln(\rho/\rho_0) \rangle_{sl}$, and stretching, $\langle \ln S \rangle_{sl}$, and σ denotes SD (*SI Appendix*, Fig. S4). (*G*) Pearson coefficients show strong correlation for both experiments (*Top*) and simulations (*Bottom*) (*SI Appendix*).

bacterial density, $\sigma_{\langle \rho/\rho_0 \rangle_{sl}}$ (*SI Appendix*, Fig. S4). The density contrast increases continuously with mean shear rate for lattice angles $\theta = 0°$ and $45°$, where the corresponding flow fields for these lattices exhibit periodic streamlines over one unit cell (Fig. 2*A*). Conversely, lattice angles having aperiodic streamlines ($\theta = 7.5°, 15°, 30°$) display a lower density contrast that varies nonmonotonically with increasing shear. To elucidate the physical origin of the bacterial density patterns, we implemented a Langevin model that accounts for the translational and rotational cell body dynamics in flow (11, 30) (*SI Appendix*). All physical parameters including cell swimming speed, V_s, and rotational diffusivity, D_r, are measured directly from experiments, leaving no fitting parameters (*Materials* and *Methods* and *SI Appendix*). The model accurately predicts the topology (Fig. 2*A*), magnitude (Fig. 1*F*), and angular dependence of the observed densification, and it enables us to make quantitative predictions beyond flow speeds achievable in our current experiments.

Hydrodynamic Bacterial Alignment Drives Densification. The coupling of not only translational but also rotational cell body dynamics to the flow is integral to swimming-cell transport (11, 30). Thus, to determine the origin of the densification, we investigate cell orientation in the vicinity of the pillars from which the density patterns spawn (Figs. 1*E* and 2*A*). The distribution of cell body orientation relative to coincident high-density streamlines (Fig. 2*B*), $p(\alpha)$, shows a strong degree of alignment (Fig. 2*D*, red curve), whereas cells on low-density streamlines are weakly aligned (Fig. 2*D*, blue curve). However, a local assessment of cell orientation reveals only a partial correlation between cell-streamline alignment and cell density (Fig. 2*C*). Local cell-streamline alignment arises from the hydrodynamic coupling of the cell body orientation to the extensional regions of the flow (31, 32), in this case emanating from two hyperbolic stagnation points on the upstream and downstream sides of the pillars, respectively (Fig. 2*C*, white arrowheads). Hydrodynamic scattering aligns elongated bacterial cells that swim into

high extension zones with streamlines that coincide with the extensional manifolds. This preferential alignment provides the mechanism for accumulation (11). However, despite the lack of local cell-streamline alignment farther downstream, high bacterial density filaments persist. Advection sweeps bacteria away from extensional zones along departing streamlines, due in part to relatively weak cell swimming speed compared with the mean flow speed ($\bar{U}_f/V_s > 1$). Thus, to understand the emergence of the high-density filaments, insight into the history of the velocity gradients experienced by cells is necessary.

Lagrangian Fluid Stretching Underpins Bacterial Density Patterns. Bacteria remain localized on streamlines for a finite time, λ, until the combined effects of hydrodynamic rotation (32), flagellar-induced tumbling (17), and Brownian rotation facilitate their escape (*SI Appendix*, Fig. S5). During this time, bacteria may be advected up to several unit cells downstream and experience a range of flow conditions. While local shear was perceived to be an indicator of bacterial accumulation in 1D flows (11), the observed cell density patterns in our Lagrangian-unsteady 2D flows do not correlate with local velocity gradients (Figs. 1E and 2A and *SI Appendix*, Fig. S1), suggesting that nonlocal effects stemming from advection dominate. The Lagrangian fluid stretching field encapsulates the integrated extension experienced over a particle's history in the flow. Stretching fields are known to be a good predictor of elongated particle alignment, even in chaotic flows (31), which suggests that stretching may also be indicative of densification (Fig. 2). Lagrangian stretching, $S(\mathbf{x}, \lambda)$, is defined (33) as the relative elongation of an initially spherical fluid particle after experiencing advection and deformation through a flow field over the time interval λ (*SI Appendix*). Fluid stretching is directly related to the finite-time Lyapunov exponent field and has been used to characterize transport in applications ranging from weather patterns to chemical reacting systems (34, 35). Stretching fields for the steady periodic lattice flows investigated here (Fig. 2E and *SI Appendix*) reveal strikingly similar topologies to the observed bacterial density patterns (Figs. 1E and 2A). Regions of high cell-streamline alignment (Fig. 2C) correspond to regions of high stretching (Fig. 2E), where local fluid deformation is strongest. However, Lagrangian stretching manifolds extend throughout the periodic lattice along streamlines due to advection (Fig. 2A). Bacterial density is thus strongly correlated with regions of high stretching (Fig. 2 F and G and *SI Appendix*), which critically relies on the elongated shape of the bacteria (Fig. 2G).

The effects of bacterial scattering are sensitive not only to the imposed mean shear rate, but also, in a further analogy with light scattering, to the incident angle of the mean flow direction, relative to the lattice (Fig. 1E). Mean flow angles exhibiting periodic streamlines ($\theta = 0°, 45°$) stretch the fluid repeatedly, when passing through the same location in the unit cell (Movies S1 and S5), reinforcing bacterial alignment and enhancing the concentration. Conversely, in flows with aperiodic streamlines ($\theta = 7.5°, 15°, 30°$; Movies S2–S4 and *SI Appendix*), the stretching field, as with the cell density, tends to a uniform spatial distribution for large mean shear rates. The emergence of bacterial densification patterns, along with their mediation by the incident angle of the flow, marks a strong departure from Brownian solutes.

Flow Hinders Lateral Bacterial Dispersion. On a larger scale, the dispersion of the scattered bacterial suspension depends upon the motility of the cells, which further distinguishes the transport properties of active and passive particles. Without flow, the persistent random walks, and thus effective diffusion coefficient, D_0, of the bacteria, are only marginally affected by the pillar lattice (*SI Appendix*, Fig. S6). However, examination of the cell displacement distribution transverse to the flow, $p(\Delta x, t)$, reveals

that the diffusive spreading of swimming bacteria is progressively hampered in the microfluidic lattice with increasing mean shear rate (Fig. 3A). This observation is corroborated by the increasingly fast decorrelation of the cells' swimming velocity with increasing mean shear rate (Fig. 3B). The velocity correlation function of the random-walking cells, $\Psi_\perp(t) = \langle v_\perp(t) \cdot v_\perp(0) \rangle$, decreases exponentially without flow due to flagellar-induced tumbling and Brownian rotational diffusion (Fig. 3B), which are modeled as rotational diffusion, D_r (*SI Appendix*). As the shear rate increases, the slow exponential decay of the cell velocity correlation gives way to rapidly decaying oscillations, which implicate hydrodynamic cell rotation through vorticity, ω, as the mechanism enhancing decorrelation (Fig. 3B and
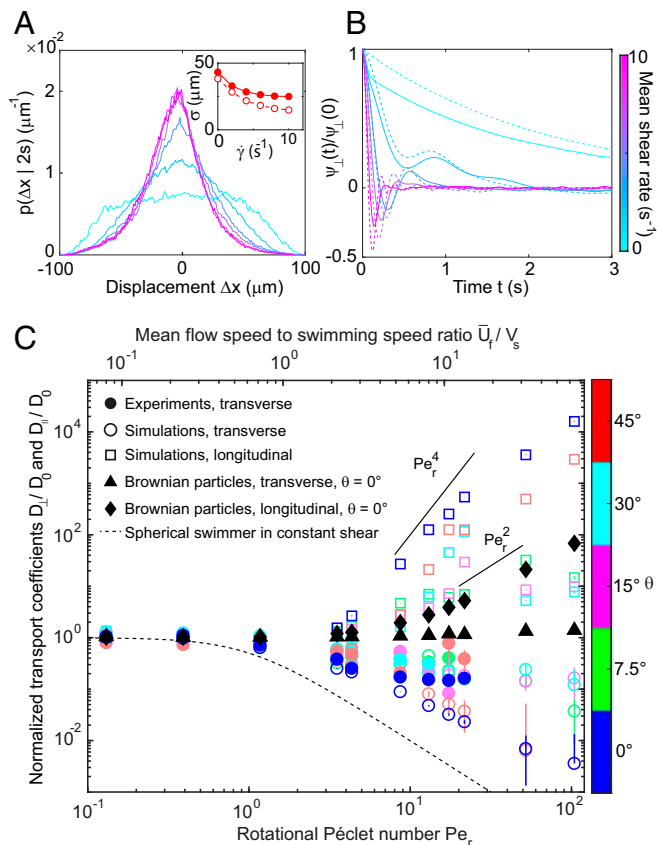
Fig. 3. Hydrodynamic cell rotation hinders transverse transport and leads to giant stream-wise dispersion. (A) Narrowing of experimental probability density functions of bacterial displacement, $p(\Delta x|2\,s)$, transverse to the mean flow direction after 2 s indicates hindered transport with increasing shear rate ($\theta = 0°$). *Inset* shows SDs, σ, of $p(\Delta x|2s)$ for experiments (solid circles) and simulations (open circles). (B) Cell velocity correlations transverse to the flow, $\Psi_\perp(t) = \langle v_\perp(t) \cdot v_\perp(0) \rangle$, show increasingly rapid temporal decorrelation with increasing mean shear ($\theta = 0°$) for experiments (solid lines) and simulations (dashed lines). (C) Effective cell transport coefficients transverse to the mean flow direction, $D_\perp$, from experiments (solid circles) and simulations (open circles), decrease with increasing rotational Péclet number, Pe_r, compared with constant diffusion for Brownian tracers (black triangles). $D_\perp$ is bounded by $D_\perp/D_0 = 1/(1 + Pe_r^2)$ (dashed black curve), which corresponds to a swimmer in constant vorticity and scales as Pe_r^{-2} for $Pe_r \gg 1$. Stream-wise cell dispersion coefficients, $D_\parallel$, from simulations (open squares) rapidly increase with Pe_r, which are bounded by Pe_r^4 compared with expected Pe_r^2 for Brownian tracer dispersion (black diamonds). Transport coefficients are normalized by D_0, measured without flow. Experimental error bars are the SD of three replicates. Simulation error bars are the maximum deviation of the Green–Kubo integral in the asymptotic range determined by a 5% convergence tolerance of the velocity correlation function (*SI Appendix*, Fig. S7).

Dehkharghani et al.

SI Appendix, Fig. S1). We examine changes in the transport coefficients as a function of the rotational Péclet number (11) based on the mean absolute vorticity, $\mathrm{Pe}_r = \langle|\omega|\rangle/2D_r$. Dispersion coefficients transverse to the flow (Fig. 3C) are obtained directly from the correlation functions of orientation through the Green–Kubo relation (36, 37), $D_\perp = \int_0^\infty \Psi_\perp(t)\,dt$ (*SI Appendix*, Fig. S7). Augmenting the flow strength, and thus the vorticity, rapidly decreases $D_\perp$ with increasing flow speed for $\mathrm{Pe}_r \gtrsim 1$, in comparison with a marginal effect for a Brownian solute (Fig. 3C and *SI Appendix*).

The lateral dispersion of bacteria depends strongly on the incident angle of the scattered suspension within the microfluidic lattice, which is rationalized by a simple model. A swimmer with rotational diffusion in constant vorticity (38, 39) yields an effective diffusion coefficient $D_\perp = D_0/(1 + \mathrm{Pe}_r^2)$ (Fig. 3C, black dashed line) (*SI Appendix*), setting the lower bound of $D_\perp$ for both our simulations and experiments. The large rotational Péclet number regime, where reduced transport occurs, also corresponds to a weak motility regime ($\bar{U}_f/V_s > 1$), where the cell is advected faster than it swims. In this context, we model an effectively nonmotile particle advected along a streamline, $\mathbf{x}(t)$, which undergoes rotational noise and experiences a vorticity that fluctuates around a mean value, $\omega(\mathbf{x}(t)) = \langle\omega\rangle_{sl} + \delta\omega(t)$. The orientation correlation function for such a particle is (*SI Appendix*)

$$\langle\mathbf{e}(t)\cdot\mathbf{e}(0)\rangle = \cos\left[\langle\omega\rangle_{sl}\,t + \int_0^t \delta\omega(\tau)\,d\tau\right] \times e^{-t/\tau_p}, \qquad \textbf{[1]}$$

where $\mathbf{e}$ is the cell swimming director and $\tau_p = 1/D_r$ is the persistence time. The magnitude of the absolute mean vorticity, $|\langle\omega\rangle_{sl}|$, is much larger for periodic streamlines compared with the aperiodic streamlines (*SI Appendix*, Fig. S8), which is at the origin of the vorticity history dependence, and thus incident angle dependence, for $D_\perp$. This model corroborates the $D_\perp \sim \mathrm{Pe}_r^{-2}$ scaling for periodic streamlines ($\theta = 0°, 45°$), while for angles with aperiodic streamlines ($\theta = 7.5°, 15°, 30°$) and random media (*SI Appendix*), $D_\perp$ decays more slowly. Despite the strong approximation of swimming cells as immotile particles, this analysis captures the variation in lateral dispersion with incident flow angle, observed in experiments and simulations (Fig. 3C).

Hindered Lateral Dispersion Enhances Longitudinal Dispersion.
We have demonstrated that the transverse dispersion of swimming bacteria is reduced (Fig. 3C), but we have yet to establish whether dispersion in active suspensions competes with or enhances the well-known longitudinal Taylor–Aris dispersion of passive Brownian particles (28, 29). The longitudinal dispersion coefficient, $D_\parallel$, rapidly increases with rotational Péclet number (Fig. 3C, $\theta = 0°$), which is far stronger than the expected $\sim \mathrm{Pe}_r^2$ scaling typical of Taylor–Aris dispersion (28, 29, 40) (Fig. 3C and *SI Appendix*). Drawing a parallel between the relatively unidirectional flow for the $\theta = 0°$ lattice and a straight duct, the dispersion of Brownian tracers is expected to scale as $D_\parallel \sim \bar{U}_f^2 R_0^2/D_m$ for $\mathrm{Pe}_r \gg 1$, where R_0 is a characteristic length and D_m is a constant molecular diffusion coefficient (28). Dispersion results from the transverse spreading of the solute across the duct, where it is swept downstream at different rates due to advection (29). However, for active, swimming cells, we have shown that the effective transverse dispersion coefficient decreases with increasing Pe_r—proportional to both mean flow speed and vorticity in Stokes flow. Taking the transverse transport coefficient as $D_m = D_\perp$, we recover a normalized dispersion coefficient that scales as $D_\parallel/D_0 \sim \mathrm{Pe}_r^4$ for $\mathrm{Pe}_r \gg 1$ (*SI Appendix*). The predicted giant Taylor–Aris dispersion coefficient scaling bounds the observed stream-wise transport coefficients for the periodic $\theta = 0°$ lattice, which exhibits an ≈ 100-fold increase in

dispersion above passive particles (Fig. 3C). Similar to Taylor–Aris dispersion (40), the observed giant longitudinal dispersion coefficient also exhibits a dependence upon the incident flow angle (Fig. 3C). However, active dispersion is systematically higher than passive Taylor dispersion, and it reflects the increase of the longitudinal dispersion coefficient, $D_\parallel$, with decreasing $D_\perp$ across various incident lattice angles (Fig. 3C) (41).

Conclusions

This work translates century-old ideas of X-ray scattering from crystalline materials (1) to the transport of active matter in an idealized porous medium, bearing curious similarities in the dependence of scattering strength on incident angle. Bacterial scattering in a microfluidic lattice reveals that flow topology, coupled with self-propulsion and cell shape, modifies the microscale spatial distribution of bacteria and impacts their macroscale transport properties, which strikingly depart from the behavior of Brownian solutes. This departure is mediated by the hydrodynamic stretching and vorticity history of the swimming cells, which are two fundamental Lagrangian properties, shown here to govern densification and dispersion, respectively. Lagrangian coherent structures have proved invaluable in understanding passive fluid transport (33–35): Our analysis shows that they offer the potential to not only characterize but also predict the transport properties of active matter in complex, dynamical fluid systems (42). In particular, the correlation of cell densification with Lagrangian stretching may be extended to random porous media (*SI Appendix*, Fig. S9) and unsteady flows, including marine turbulence, where predicting cell transport is both challenging and important to large-scale bio-oceanography modeling (21, 24, 43). The emergent heterogeneous cell distributions at the pore scale will inform our understanding of microbial function and biome dynamics in processes ranging from biofilm formation (44) to niche partitioning (45). Harnessing these novel transport properties could inspire new methods for cell separation (46) or tailoring dispersion (29) for applications in water filtration (47), remediation (48–50), and control of active matter (51, 52).

Materials and Methods

Bacterial Culturing. Wild-type *B. subtilis* bacteria (OI1085) were cultured by inoculating 5 mL of Cap Assay Minimal (CAM) motility medium with cells obtained from a frozen glycerol stock (53). Cells were grown initially for 12 h (37 °C, 250 rpm) to an optical density $\mathrm{OD}_{600} = 0.05$ and then subcultured (100 μL in 5 ml of CAM) and regrown for 10 h to $\mathrm{OD}_{600} = 0.1$. Before experiments, bacterial suspensions were diluted 10 times in CAM medium to $\approx 6.5 \times 10^6$ cells/mL, making cell–cell interactions negligible.

Microfabrication and Microfluidic Experiments. Polydimethylsiloxane (PDMS) microfluidic channels were fabricated through soft lithography (54) and plasma bonded to standard glass microscope slides. The 100-μm high channels had an overall length and width of 40 mm and 3.6 mm, respectively. The square lattice of circular pillars (65 μm diameter, 120 μm spacing) occupied the central 10 mm of five different microchannels, which were prepared with lattices oriented at angles $\theta = 0°, 7.5°, 15°, 30°,$ and $45°$ relative to the mean flow direction. Cell suspensions were driven with a syringe pump (Harvard Apparatus) at rates $Q = 0, 0.03, 0.09, 0.27, 0.81, 1, 2, 3, 4, 5$ μL/min in random order to avoid systematic errors and allowed to reach steady state for 60 s, before acquiring image data. Before and after each experiment, the flow was halted, and cells were imaged in the open region of the channel devoid of pillars to measure cell swimming speed, V_s, and effective rotational diffusivity, D_r. The full set of experiments for all lattice angles and flow rates was repeated three times on different days with freshly cultured bacteria.

Cell Imaging and Tracking. Imaging was performed at middepth in the microchannel pillar array test section far from side walls and four or more lattice spacings from the end of the test section. Cells were imaged using phase-contrast microscopy on an inverted microscope (Nikon Ti-E; 10×, 0.3 NA objective). For each experimental condition, a 4,000-frame video was recorded at 45 fps (Zyla sCMOS camera; Andor Technology).

Bacteria were tracked using a custom predictive particle-tracking algorithm (MATLAB; MathWorks), yielding ≈15,000 cell trajectories per video. Cell detection within ≈8 μm of the pillar surfaces was unreliable due to strong light scattering, and thus these regions were omitted from further analysis.

Periodic Cell Density Averaging. The full field of view comprises ∼8 × 7 unit cells (120 μm × 120 μm) with vertices based on pillar centers. From cell-tracking data, bacterial positions are determined relative to their local unit cell. The unit cell space is binned into a 60 × 60 grid, and the cell counts are tallied for each bin over the course of the experiment. Cell counts are normalized by the total number of bacteria giving the 2D bacterial probability density, ρ. We further normalize ρ by the average value of the bacterial density, ρ_0, and present data as a 2×2 tiling of four unit cells for both experimental and simulation results (Figs. 1 and 2).

1. Authier A (2013) *Early Days of X-Ray Crystallography* (Oxford Univ Press, Oxford, UK).
2. Alexander GP, Pooley CM, Yeomans JM (2008) Scattering of low-Reynolds-number swimmers. *Phys Rev E* 78:045302(R).
3. Drescher K, Dunkel J, Cisneros LH, Ganguly S, Goldstein RE (2011) Fluid dynamics and noise in bacterial cell-cell and cell-surface scattering. *Proc Natl Acad Sci USA* 108:10940–10945.
4. Kantsler V, Dunkel J, Blayney M, Goldstein RE (2014) Rheotaxis facilitates upstream navigation of mammalian sperm cells. *eLife* 3:e02403.
5. Sipos O, Nagy K, Di Leonardo R, Galajda P (2015) Hydrodynamic trapping of swimming bacteria by convex walls. *Phys Rev Lett* 114:258104.
6. Contino M, Lushi E, Tuval I, Kantsler V, Polin M (2015) Microalgae scatter off solid surfaces by hydrodynamic and contact forces. *Phys Rev Lett* 115:258102.
7. Li G, Tang JX (2009) Accumulation of microswimmers near a surface mediated by collision and rotational Brownian motion. *Phys Rev Lett* 103:078101.
8. Guasto JS, Rusconi R, Stocker R (2012) Fluid mechanics of planktonic microorganisms. *Annu Rev Fluid Mech* 44:373–400.
9. Stocker R (2012) Marine microbes see a sea of gradients. *Science* 338:628–633.
10. Durham WM, Kessler JO, Stocker R (2009) Disruption of vertical motility by shear triggers formation of thin phytoplankton layers. *Science* 323:1067–1070.
11. Rusconi R, Guasto JS, Stocker R (2014) Bacterial transport suppressed by fluid shear. *Nat Phys* 10:212–217.
12. Ford RM, Harvey RW (2007) Role of chemotaxis in the transport of bacteria through saturated porous media. *Adv Water Resour* 30:1608–1617.
13. Riffell JA, Zimmer RK (2007) Sex and flow: The consequences of fluid shear for sperm egg interactions. *J Exp Biol* 210:3644–3660.
14. Nadell CD, Drescher K, Foster KR (2016) Spatial structure, cooperation, and competition in bacterial biofilms. *Nat Rev Microbiol* 14:589–600.
15. Pandey PK, Kass PH, Soupir ML, Biswas S, Singh VP (2014) Contamination of water resources by pathogenic bacteria. *AMB Express* 4:51.
16. Tufenkji N (2007) Modeling microbial transport in porous media: Traditional approaches and recent developments. *Adv Water Resour* 30:1455–1469.
17. Berg HC, Brown DA (1972) Chemotaxis in Escherichia coli analysed by three-dimensional tracking. *Nature* 239:500–504.
18. Polin M, Tuval I, Drescher K, Gollub JP, Goldstein RE (2009) Chlamydomonas swims with two "gears" in a eukaryotic version of run-and-tumble locomotion. *Science* 325:487–490.
19. Howse JR, et al. (2007) Self-motile colloidal particles: From directed propulsion to random walk. *Phys Rev Lett* 99:048102.
20. Long T, Ford RM (2009) Enhanced transverse migration of bacteria by chemotaxis in a porous T-sensor. *Environ Sci Technol* 43:1546–1552.
21. Taylor JR, Stocker R (2012) Trade-offs of chemotactic foraging in turbulent water. *Science* 338:675–679.
22. Kessler JO (1985) Hydrodynamic focusing of motile algal cells. *Nature* 313:218–220.
23. Ten Hagen B, Wittkowski R, Löwen H (2011) Brownian dynamics of a self-propelled particle in shear flow. *Phys Rev E* 84:031105.
24. Durham WM, et al. (2013) Turbulence drives microscale patches of motile phytoplankton. *Nat Commun* 4:2148.
25. De Lillo F, et al. (2014) Turbulent fluid acceleration generates clusters of gyrotactic microorganisms. *Phys Rev Lett* 112:044502.
26. Bees MA, Croze OA (2010) Dispersion of biased swimming micro-organisms in a fluid flowing through a tube. *Proc R Soc A Math Phys Eng Sci* 466:2057–2077.
27. Le Borgne T, Dentz M, Villermaux E (2013) Stretching, coalescence, and mixing in porous media. *Phys Rev Lett* 110:204501.
28. Aris R (1956) On the dispersion of a solute in a fluid flowing through a tube. *Proc R Soc A Math Phys Eng Sci* 235:67–77.
29. Aminian M, Bernardi F, Camassa R, Harris DM, McLaughlin RM (2016) How boundaries shape chemical delivery in microfluidics. *Science* 354:1252–1256.
30. Pedley TJ, Kessler JO, Pedley T (1992) Hydrodynamic phenomena in suspensions of swimming microorganisms. *Annu Rev Fluid Mech* 24:313–358.
31. Parsa S, et al. (2011) Rotation and alignment of rods in two-dimensional chaotic flow. *Phys Fluids* 23:043302.
32. Jeffery GB (1922) The motion of ellipsoidal particles immersed in a viscous fluid. *Proc R Soc A Math Phys Eng Sci* 102:161–179.
33. Voth GA, Haller G, Gollub JP (2002) Experimental measurements of stretching fields in fluid mixing. *Phys Rev Lett* 88:254501.
34. Haller G (2015) Lagrangian coherent structures. *Annu Rev Fluid Mech* 47:137–162.
35. Arratia PE, Gollub JP (2006) Predicting the progress of diffusively limited chemical reactions in the presence of chaotic advection. *Phys Rev Lett* 96:024501.
36. Green MS (1954) Markoff random processes and the statistical mechanics of time-dependent phenomena. II. Irreversible processes in fluids. *J Chem Phys* 22:398–413.
37. Kubo R (1957) Statistical-mechanical theory of irreversible processes. I. General theory and simple applications to magnetic and conduction problems. *J Phys Soc Jpn* 12:570–586.
38. Friedrich BM, Jülicher F (2008) The stochastic dance of circling sperm cells: Sperm chemotaxis in the plane. *New J Phys* 10:123025.
39. Bearon RN, Pedley TJ (2000) Modelling run-and-tumble chemotaxis in a shear flow. *Bull Math Biol* 62:775–791.
40. Amaral Souto HP, Moyne C (1997) Dispersion in two-dimensional periodic porous media part II. Dispersion tensor. *Phys Fluids* 9:2253–2263.
41. Zaks MA, Nepomnyashchy A (2018) Subdiffusive and superdiffusive transport in plane steady viscous flows. *Proc Natl Acad Sci USA* 115:201717225.
42. Khurana N, Ouellette NT (2012) Interactions between active particles and dynamical structures in chaotic flow. *Phys Fluids* 24:091902.
43. Ward BA, Dutkiewicz S, Follows MJ (2014) Modelling spatial and temporal patterns in size-structured marine plankton communities: Top-down and bottom-up controls. *J Plankton Res* 36:31–47.
44. Hall-Stoodley L, Costerton JW, Stoodley P (2004) Bacterial biofilms: From the natural environment to infectious diseases. *Nat Rev Microbiol* 2:95–108.
45. Hunt DE, et al. (2008) Resource partitioning and sympatric differentiation among closely related bacterioplankton. *Science* 320:1081–1085.
46. Kim SC, et al. (2017) Broken flow symmetry explains the dynamics of small particles in deterministic lateral displacement arrays. *Proc Natl Acad Sci USA* 114:E5034–E5041.
47. Sobsey MD, Stauber CE, Casanova LM, Brown JM, Elliott MA (2008) Point of use household drinking water filtration: A practical, effective solution for providing sustained access to safe drinking water in the developing world. *Environ Sci Technol* 42:4261–4267.
48. Dzionek A, Wojcieszyńska D, Guzik U (2016) Natural carriers in bioremediation: A review. *Electron J Biotechnol* 23:28–36.
49. Khan FI, Husain T, Hejazi R (2004) An overview and analysis of site remediation technologies. *J Environ Manage* 71:95– 122.
50. Das K, Mukherjee AK (2007) Crude petroleum-oil biodegradation efficiency of Bacillus subtilis and Pseudomonas aeruginosa strains isolated from a petroleum-oil contaminated soil from North-East India. *Bioresour Technol* 98:1339–1345.
51. Palacci J, Sacanna S, Steinberg AP, Pine DJ, Chaikin PM (2013) Living crystals of light-activated colloidal surfers. *Science* 339:936–940.
52. Morin A, Desreumaux N, Caussin JB, Bartolo D (2017) Distortion and destruction of colloidal flocks in disordered environments. *Nat Phys* 13:63–67.
53. Marcos, Fu H, Powers TR, Stocker R (2012) Bacterial rheotaxis. *Proc Natl Acad Sci USA* 109:4780–4785.
54. Xia Y, Whitesides GM (1998) Soft lithography. *Annu Rev Mater Sci* 28:153–184.